PHYSICAL REVIEW A **105**, 053503 (2022)

Broadband ultrawide-angle laser-plasma microwave antennas

A. V. Mitrofanov,[1,2,3,4] D. A. Sidorov-Biryukov,[1,2,3,5] M. V. Rozhko,[1,2] N. V. Erukhimova,[2] A. A. Voronin,[1,2,5]
M. M. Nazarov,[3] A. B. Fedotov,[1,2,5] and A. M. Zheltikov[6]

[1] *Physics Department, M. V. Lomonosov Moscow State University, Moscow 119992, Russia*
[2] *Russian Quantum Center, Skolkovo, Moscow Region 143025, Russia*
[3] *Kurchatov Institute National Research Center, Moscow 123182, Russia*
[4] *Institute of Laser and Information Technology–Branch of FSRC "Crystallography and Photonics,"*
Russian Academy of Science, Shatura, 140700 Russia
[5] *Kazan Quantum Center, A. N. Tupolev Kazan National Research Technical University, 420126 Kazan, Russia*
[6] *Department of Physics and Astronomy, Texas A&M University, College Station, Texas 77843, USA*

(Received 20 October 2021; accepted 23 March 2022; published 4 May 2022)

Electric-current transients driven by high-peak-power midinfrared laser pulses are shown to provide a source of broadband current, wide-angle microwave-terahertz radiation, whose spectral, spatial, and polarization properties can be adequately understood from a perspective of impulsively driven antenna radiation. When suitably tailored, such laser-driven antennas are shown to generate bright microwave-terahertz pulses with energies in the range of tens of microjoules and ultrawide-angle radiation patterns extending to obtuse angles well beyond the broadside plane, with a considerable radiation flux detected at angles $\theta > 125^\circ$ relative to the direction of the driver beam. Polarization of microwave radiation from laser-driven plasmas is shown to bear clear signatures of the symmetry of transient plasma currents, providing a sensitive probe for ultrafast laser-plasma interactions.

DOI: 10.1103/PhysRevA.105.053503

I. INTRODUCTION

Ultrafast laser-driven plasma electrodynamics harbors a vast variety of light-matter interaction scenarios, providing a rapidly expanding interface between plasma physics, ultrafast optical science, and strong-field laser physics [1–4]. Pushing the frontiers of fundamental research and advanced photonic technologies are the ideas of laser-plasma particle accelerators [5–11], relativistic laser-plasma physics [12–19], and laser-plasma sources of high-brightness attosecond pulses [20–24].

Of special interest for laboratory-scale optical science are ultrafast laser-driven plasma nonlinearities that lead to complex spectral and temporal transformations of laser field waveforms, giving rise to extremely short and bright bursts of up- and down-converted electromagnetic radiation [25–33]. While optical nonlinearities of bound electrons in atoms and ions give rise to a vast variety of interesting coherent wave-mixing scenarios in ultrafast laser-plasma electrodynamics, enabling high-order harmonic generation, as well as efficient frequency up- and down-conversion [2,34], it is the transient currents of electric charge that short laser pulses drive as a part of ultrafast laser-plasma interactions that are largely responsible for an extraordinarily broad bandwidth of laser-plasma optical nonlinearities [27–31,35]. In many laser-plasma interaction settings, such intrinsically broadband optical nonlinearities provide a source of radiation whose frequency spectrum can in certain regimes span from the x ray all the way down to the microwave range [33,34,36,37] well beyond the limits set out by the canonical, textbook picture of nonlinear-polarization-enabled wave-mixing dynamics. Such ultrabroadband nonlinear electrodynamics sets the scene for the physics of subcycle electromagnetic field waveforms and attosecond technologies, as well as terahertz and microwave photonics.

Although the speeds of the charged particles that constitute plasma-current sources of optical nonlinearities in a vast class of moderate-intensity laser-plasma interaction settings are well below the speed of light, the ionization front that sets these charges in motion, thus inducing plasma currents, propagates at the speed of light as it rides on the back of the laser pulse that gives rise to plasma generation via ultrafast photoionization [38–40]. An important question to ask in this context is to what extent the fundamental electrodynamics of relativistic charges can be extended to understand the properties of radiation emitted by laser-driven plasma currents. Specifically, microwave and terahertz (THz) generation in laser-plasma settings has been shown to exhibit readily recognizable signatures of bremsstrahlung, Cherenkov, and transition radiation [38–42], offering useful insights into the electrodynamics behind low-frequency radiation by laser-driven plasmas.

Here, we seek a deeper understanding of the map between the symmetry of laser-driven plasma currents and the properties of secondary radiation by such currents as dictated by relativistic-charge electrodynamics. We show that electric-current transients driven by high-peak-power midinfrared laser pulses can provide a source of broadband, wide-angle radiation whose spectrum spans over a remarkably broad range, stretching across the entire THz region and extending deeply into the microwave range. As one of

2469-9926/2022/105(5)/053503(12)

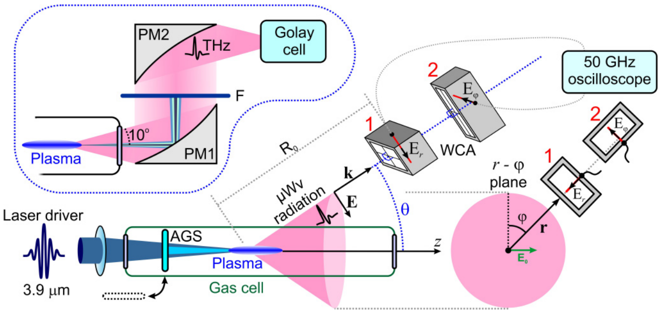

FIG. 1. Experimental setup: AGS, $AgGaS_2$ crystal for second-harmonic generation; E and k, the electric field and the wave vector of the microwave radiation field; WCA, waveguide-to-coaxial adapter, with a coaxial probe shown in red. Also shown are the two settings of the WCA, with the WCA coaxial probe set to detect the E_r (1) and E_φ (2) components of the microwave field and with a linearly polarized mid-IR driver field E_0. Shown in the inset is a diagram of microwave-THz output energy measurements: PM1, PM2, off-axis parabolic mirrors; F, stack of microwave-THz filters.

the key findings of this study, extending the understanding of ultrafast laser-plasma physics beyond the earlier work, we show that the main spectral, temporal, spatial, and polarization properties of this THz-microwave emission can be adequately understood from a perspective of impulsively driven antenna radiation. We present a detailed quantitative comparison of closed-form solutions for the radiation field emitted by such a pulsed antenna with the results of laser-plasma experiments, showing that the predictions of pulsed-antenna analysis agree very well with experimental results, thus suggesting a physically clear, intuitive picture of THz-microwave generation in laser plasmas and laser filaments. We demonstrate that, when suitably tailored, laser-driven pulsed antennas can generate bright microwave-THz pulses with energies in the range of tens of microjoules and ultrawide-angle radiation patterns extending to obtuse angles well beyond the broadside plane, with a considerable radiation flux detected at angles $\theta > 125^\circ$ relative to the direction of the driver beam. Polarization of microwave radiation from laser-driven plasmas is shown to bear clear signatures of the symmetry of transient plasma currents, providing a sensitive probe for ultrafast laser-plasma interactions.

II. EXPERIMENT

A. Laser driver

Serving as a source of a mid-IR driver field in our experiments (Fig. 1) is a pulse-compressed output of a three-stage optical parametric chirped-pulse amplifier (OPCPA) [43], delivering mid-IR field waveforms with a central wavelength $\lambda_0 \approx 3.9\,\mu m$, a pulse width $\tau_0 \approx 80\,\text{fs}$, and a pulse energy up to $W_0 \approx 35\,\text{mJ}$ [44].The mid-IR OPCPA output is focused into a gas cell with a 50-cm-focal-length lens (Fig. 1). The gas pressure p inside the gas cell is varied from 10^{-7} up to 1.0 bar via the combined use of a turbomolecular vacuum pump and a rotary variable displacement dry-vacuum booster. The moisture content within the gas cell, h, is controlled with an evaporative humidifier and is monitored with a resistive hygrometer (Fisher Scientific or equivalent). All the measurements presented below in this paper have been performed at $h \approx 50\%$.

For two-color-driver laser-plasma experiments, a 0.5-mm-thick $AgGaS_2$ crystal (AGS in Fig. 1) is placed right behind the CaF_2 gas-cell entrance window to generate the second harmonic (SH) of the $\lambda_0 \approx 3.9\,\mu\text{m}$ driver, yielding radiation with a central wavelength $\lambda_{SH} = \lambda_0/2$. In a typical laser-plasma experiment with a two-color driver, the energy of the SH output, E_{SH}, is set within the range of ≈ 0.1–$0.3\,\text{mJ}$ and its phase is shifted by $\pi/2$ relative to the phase of the $\lambda_0 \approx 3.9\,\mu\text{m}$ driver. Both the 3.9-μm field and its second harmonic are linearly polarized in our experiments, as verified by careful polarization measurements. In single-color experiments, the AGS crystal is removed from the gas cell (as sketched in Fig. 1). The focused single-color (the 3.9-μm-only OPCPA output) or two-color (the 3.9-μm OPCPA output and its SH) field drives a gas target, giving rise to broadband, supercontinuum radiation, whose spectrum spans from the microwave range to at least the vacuum ultraviolet [33].

B. Microwave-THz detection

Broadband microwave detection is performed in our experiments (Fig. 1) with the use of five waveguide-to-coaxial adapters (WCAs) [42], placed at a variable distance R_0 from the laser-plasma source of microwave radiation and oriented at a variable angle θ relative to the driver beam axis (the z axis in Fig. 1). The WCAs used in our experiments were intended to detect radiation within the frequency ranges from $\nu = \omega/(2\pi) \approx 3.0$ to 15 GHz (WCA1), $\approx$5.0 to 19 GHz (WCA2), $\approx$8.0 to 25 GHz (WCA3), $\approx$13 to 33 GHz (WCA4), and $\approx$30 to 50 GHz (WCA5). The WCA readout is analyzed and recorded with a 50-GHz oscilloscope.

The radiation patterns of the microwave field are studied by measuring the microwave laser-plasma output as a function of the angle θ that the direction to the WCA detector makes with the driver beam propagation axis (the z axis, Fig. 1). Polarization of microwave radiation is analyzed by rotating the WCA about the normal to its aperture and by aligning its coaxial probe (shown red in Fig. 1) in such a way, i.e., at such an angle φ relative to $\mathbf{r}$ (Fig. 1), as to isolate the significant field components characterizing polarization modes of microwave radiation. Specifically, with the WCA coaxial-cable probe aligned with $\mathbf{r}$ (detection setting 1 in Fig. 1), the WCA will isolate the E_r component of the microwave field. When the WCA probe is oriented along the normal to $\mathbf{r}$ in the $r\varphi$ plane, on the other hand, the orthogonal field component, E_φ, is isolated (detection setting 2 in Fig. 1).

The spectral intensity distribution within microwave-THz radiation is analyzed with the use of carefully calibrated stacks of microwave-THz attenuators placed in front of a Golay cell (the inset in Fig. 1), enabling high-sensitivity radiation detection within the range from $\sim$40 GHz up to 300 THz. In such measurements, the supercontinuum output of laser-driven plasmas is first transmitted through a 3-mm-thick polypropylene filter, which blocks the IR-to-UV part of supercontinuum radiation. The microwave-to-THz part of the supercontinuum (SC) field that passes through this filter then undergoes an adjustable frequency-dependent attenuation in a stack of slides made of materials with carefully calibrated thicknesses and

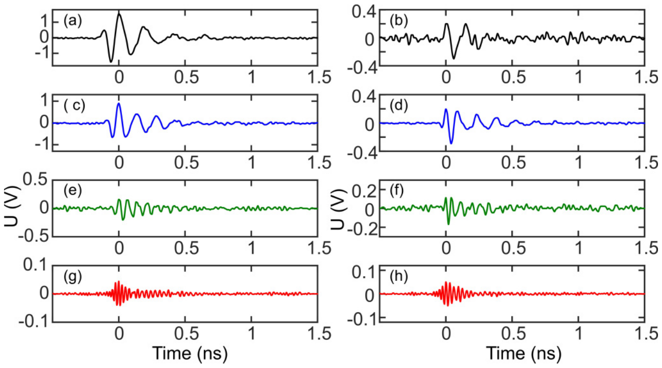

FIG. 2. Traces of microwave field waveforms recorded with WCA1 (a,b), WCA2 (c,d), WCA4 (e,f), and WCA 5 (g,h) set at $\varphi = 0^\circ$ and $\theta \approx 53^\circ$ in experiments with a single-color laser driver with $\lambda_0 \approx 3.9\,\mu$m, $W_0 \approx 15$ mJ, and $\tau_0 \approx 80$ fs in a gas cell filled with atmospheric air at pressure $p \approx 2$ mbar (a,c,e,g) and 1000 mbar (b,d,f,h).

well-characterized attenuation spectra. Standard examples of materials used for an adjustable attenuation of microwave-to-THz radiation include high-density polyethylene (HDPE), 2-g/cm^3 polytetrafluoroethylene (PTFE), polymethylpentene (TPX), polymethyl methacrylate (PMMA), and 100-g/m^2 paper.

III. RADIATION PATTERNS AND POLARIZATION PROPERTIES OF MICROWAVE RADIATION

As the laser driver field propagates through the gas cell, it gives rise to broadband microwave-THz radiation. In Figs. 2(a)–2(h), we present typical polarization-resolved time traces of microwave field waveforms recorded with WCA detectors designed for different frequency ranges. The spectra retrieved from such traces, measured within a broad range of distances R_0, angles θ, gas pressures p, and laser pulse energies W_0 are shown in Figs. 3–6. In both one- and two-color laser-plasma settings, the microwave readouts Φ of all the WCA detectors were found to closely follow the $1/R_0^2$ scaling with the distance R_0 from the laser-plasma source [Figs. 7(a) and 7(b)].

Polarization dependences of the microwave output and its radiation patterns $\Phi(\theta)$ in one- and two-color experiments are, however, distinctly different (Figs. 8–10). In single-color laser-plasma studies, the angular profile of the microwave output $\Phi(\theta)$ features well-resolved dips in the direction of driver propagation [Figs. 9(b) and 10(a)–10(c)] alongside off-axis peaks, which tend to shift as functions of the gas pressure p and radiation frequency ω [Figs. 10(a)–10(c)]. In two-color experiments, on the other hand, the $\Phi(\theta)$ profiles peak in the direction of driver beam propagation, i.e., at $\theta = 0$, rolling off as θ is increased [Figs. 9(a)and 10(d)–10(f)]. Furthermore, the microwave output detected in single-color experiments is found to be dominated by a radially polarized mode, with E_r being virtually independent of φ and with E_φ being orders of magnitude weaker than E_r [Figs. 8(a) and 8(b)]. In two-color experiments, on the other hand, linearly polarized microwave radiation is observed in a broad range of gas pressures and laser field intensities [Fig. 8(c)].

Presented in Fig. 8(d) is the microwave-THz output energy measured with the Golay cell behind a suitable stack of spectral filters (the inset in Fig. 1) as a function of the gas pressure p for a variety of atomic and molecular gases—Kr,

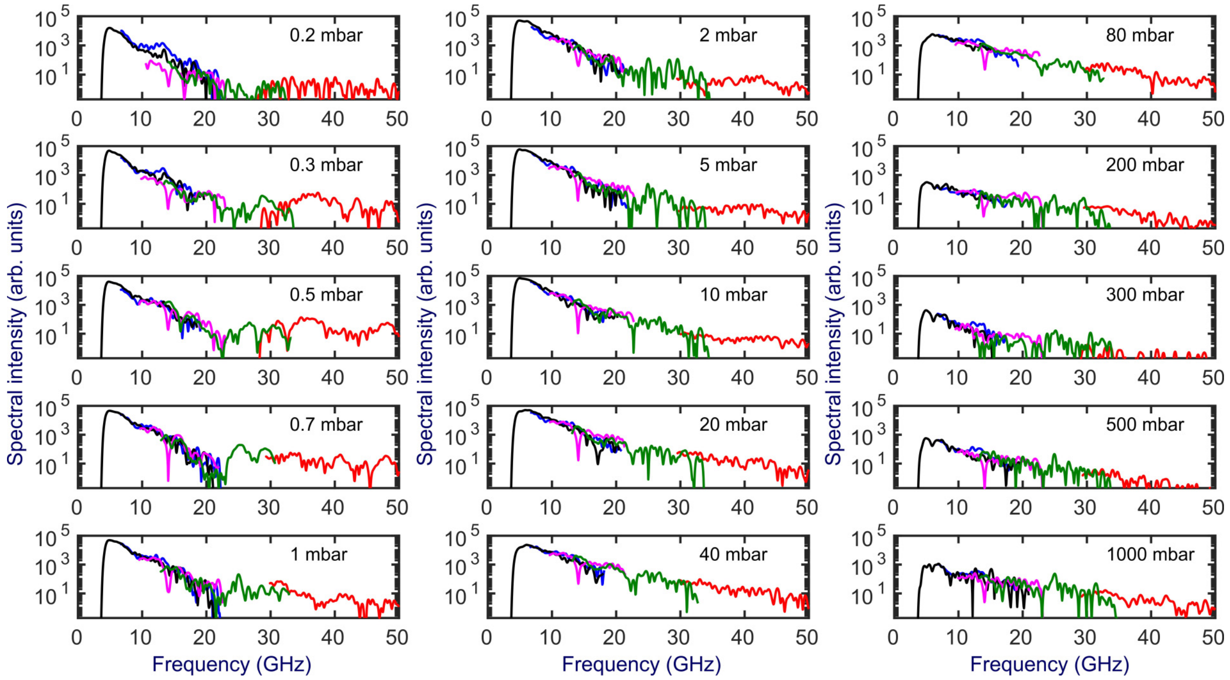

FIG. 3. The spectra of microwave radiation retrieved from WCA traces recorded with WCA1 (black, from 3.0 to 15 GHz), WCA2 (blue, from 5.0 to 19 GHz), WCA3 (pink, from 8.0 to 25 GHz), WCA4 (green, from 13 to 33 GHz), and WCA 5 (red, from 30 to 50 GHz) set at $\varphi = 0^\circ$ and $\theta \approx 53^\circ$ in experiments with a single-color laser driver with $\lambda_0 \approx 3.9\,\mu$m, $W_0 \approx 15$ mJ, and $\tau_0 \approx 80$ fs in a gas cell filled with atmospheric air at pressure p as shown in the panel.

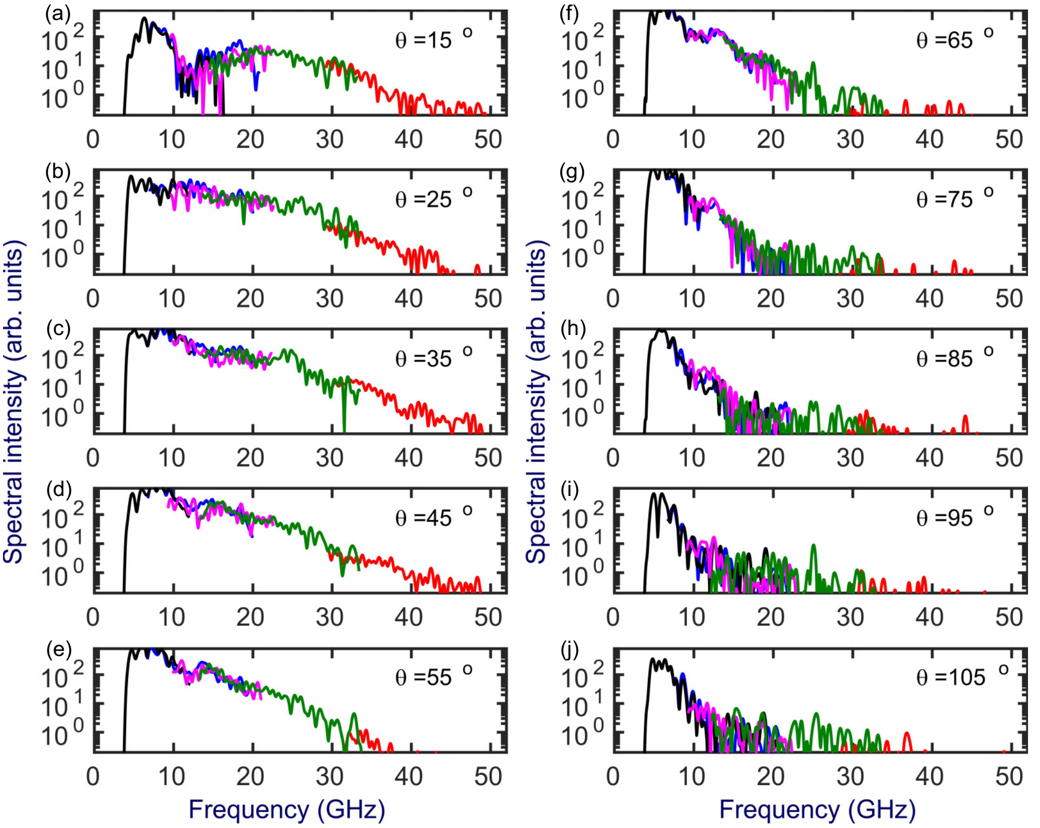

FIG. 4. The spectra of microwave radiation retrieved from WCA traces recorded with WCA1 (black, from 3.0 to 15 GHz), WCA2 (blue, from 5.0 to 19 GHz), WCA3 (pink, from 8.0 to 25 GHz), WCA4 (green, from 13 to 33 GHz), and WCA 5 (red, from 30 to 50 GHz) in experiments with a single-color laser driver with $\lambda_0 \approx 3.9\,\mu$m, $W_0 \approx 11$ mJ, and $\tau_0 \approx 80$ fs in a gas cell filled with atmospheric air at pressure $p \approx 50$ mbar for $\varphi = 0^\circ$, and $\theta \approx 15^\circ$ (a), 25 ° (b), 35 ° (c), 45 ° (d), 55 ° (e), 65 ° (f), 75 ° (g), 85 ° (h), 95 ° (i), and 105 ° (j), as specified in the panels.

N_2, air—driven by the two-color laser field. The rationale for choosing this selection of gases is threefold. First, experiments with this selection of gases are aimed at showing that laser-ionization-assisted microwave-THz generation can take place in both purely atomic and purely molecular gases, such as Kr and N_2, as well as in gas mixtures, such as air. Second, experiments within this assortment of gases could help detect any features of microwave-THz generation that would be specific to the molecular part of the optical nonlinearity of a gas target, including the signatures of the Raman effect

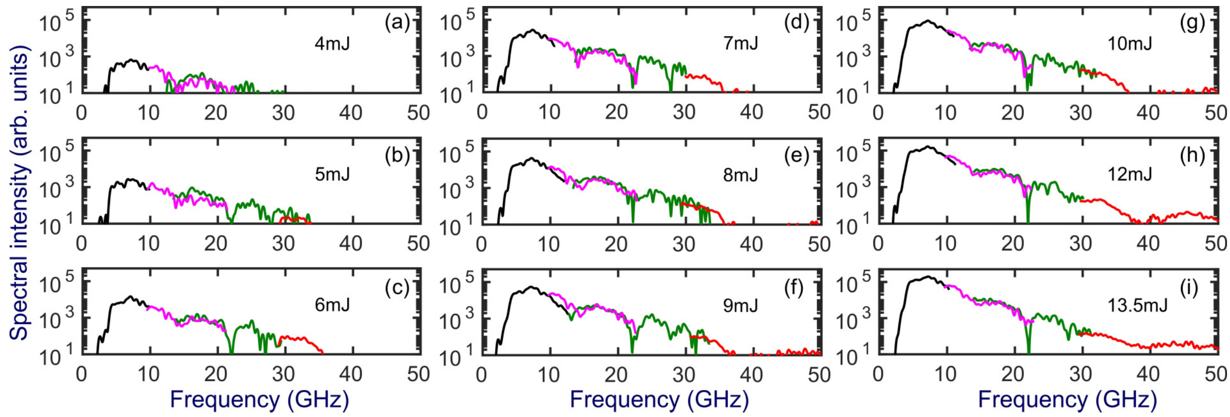

FIG. 5. The spectra of microwave radiation retrieved from WCA traces recorded with WCA1 (black, from 3.0 to 15 GHz), WCA3 (pink, from 8.0 to 25 GHz), WCA4 (green, from 13 to 33 GHz), and WCA 5 (red, from 30 to 50 GHz) in experiments with a single-color laser driver with $\lambda_0 \approx 3.9\,\mu$m and $\tau_0 \approx 80$ fs in a gas cell filled with atmospheric air at pressure $p \approx 20$ mbar for $\varphi = 0^\circ$, $\theta \approx 35^\circ$, and $W_0 \approx 4$ mJ (a), 5 mJ (b), 6 mJ (c), 7 mJ (d), 8 mJ (e), 9 mJ (f), 10 mJ (g), 12 mJ (h), and 13.5 mJ (i), as specified in the panels.

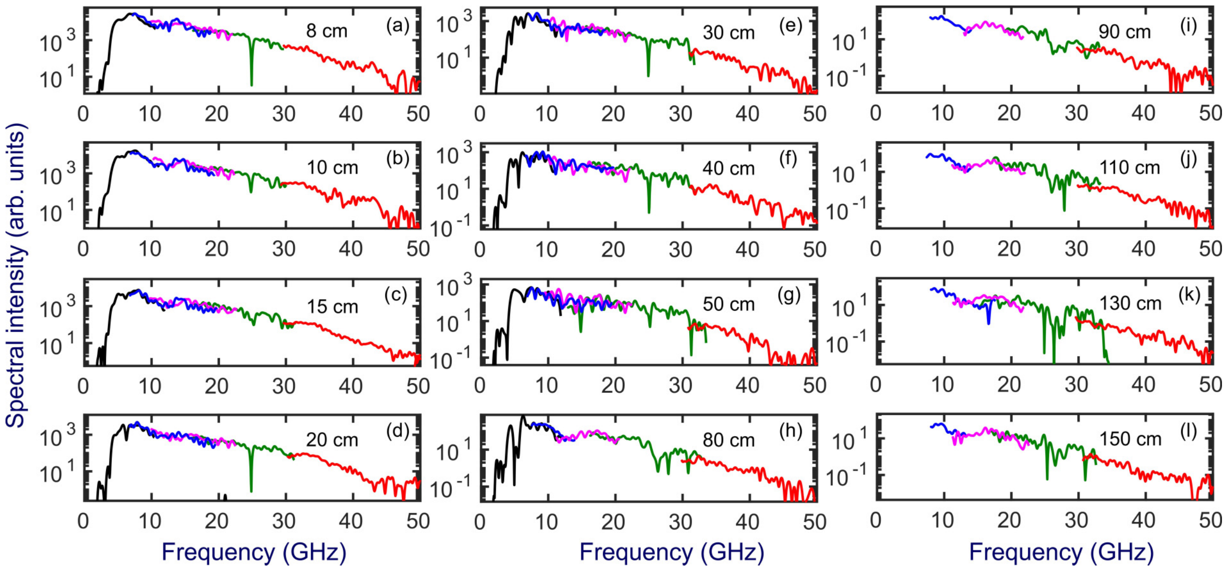

FIG. 6. The spectra of microwave radiation retrieved from WCA traces recorded with WCA1 (black, from 3.0 to 15 GHz), WCA2 (blue, from 5.0 to 19 GHz), WCA3 (pink, from 8.0 to 25 GHz), WCA4 (green, from 13 to 33 GHz), and WCA 5 (red, from 30 to 50 GHz) in experiments with a single-color laser driver with $\lambda_0 \approx 3.9\,\mu$m, $W_0 \approx 12$ mJ, and $\tau_0 \approx 80$ fs in a gas cell filled with atmospheric air at pressure $p \approx 50$ mbar for $\varphi = 0^\circ$, $\theta \approx 40^\circ$, and the distance R_0 between the detector and the laser-plasma radiation set at 8 cm (a), 10 cm (b), 15 cm (c), 20 cm (d), 30 cm (e), 40 cm (f), 50 cm (g), 80 cm (h), 90 cm (i), 110 cm (j), 130 cm (k), and 150 cm (l).

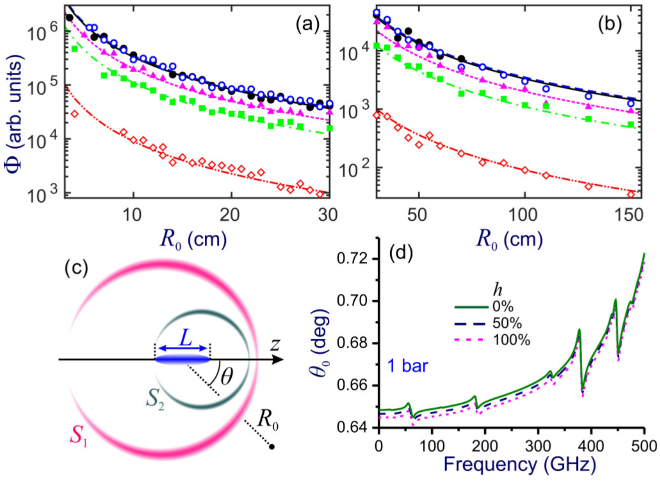

FIG. 7. (a,b) The microwave output as a function of the distance between the detector and the laser-plasma source measured with a WCA1 (black filled circles), WCA2 (blue open circles), WCA3 (pink triangles), WCA4 (green boxes), and WCA5 (red open diamonds) for $\varphi = 0$, $p = 50$ mbar of air, and $\theta = 40^\circ$ (WCA1 – WCA4 measurements) and $\theta = 30^\circ$ (WCA5). The lines show the best D^2 fits of the experimental dependences. (c) Transient-antenna laser-plasma radiation driven by a traveling wave of electric current, with opposite-polarity spherical-wave field waveforms (pink circle S_1 and blue circle S_2) radiated by an impulsively driven current near the $z = 0$ and $z = L$ plasma end points. (d) The angle θ_0 of the Cherenkov emission cone for microwave–sub-THz radiation of frequency ν (shown along the abscissa axis) emitted by an electric current as defined by Eq. (1) in atmospheric air at $T = 25\,^\circ$C, $\rho = 50\%$, $p = 1$ bar, and $h = 0\%$ (green solid line), 50% (blue dashed line), and 100% (pink dotted line), with the central wavelength of the laser driver set at $\lambda_0 = 3.9\,\mu$m.

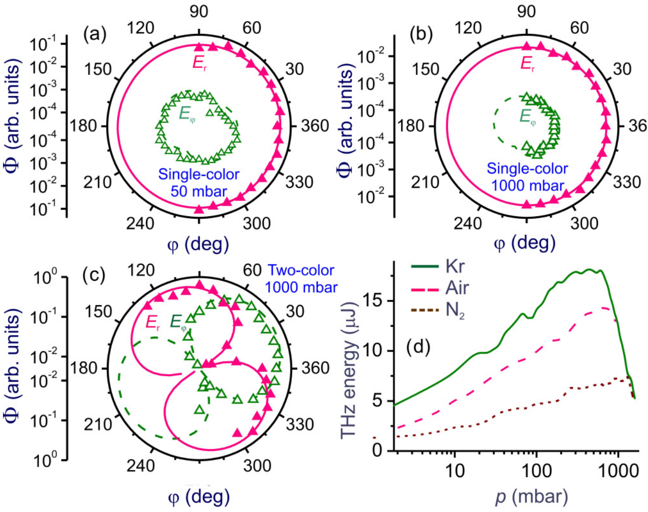

FIG. 8. (a–c) The E_r (pink filled triangles) and E_φ (green open triangles) components of the microwave field generated by a single-color driver with $\lambda_0 \approx 3.9\,\mu$m, $E_0 \approx 15$ mJ, and $\tau_0 \approx 80$ fs (a,b) and two-color laser driver with $\lambda_0 \approx 3.9\,\mu$m, $E_0 \approx 15$ mJ, $\lambda_{\rm SH} = \lambda_0/2$, $E_{\rm SH} \approx 0.1$ mJ, $\phi_{\rm SH} = \pi/2$, and $\tau_0 \approx 80$ fs (c) as functions of φ measured with WCA5 at $p \approx 50$ mbar (a), and 1000 mbar (b,c) of air. Shown with the solid and dashed lines are the best fits of the experimental data with φ dependences as expected for a pulsed antenna driven by longitudinal (a,b) and transverse (c) electric currents. (d) The energy of microwave-to-THz SC generated by a two-color laser driver with a central wavelength $\lambda_0 \approx 3.9\,\mu$m, pulse width $\tau_0 \approx 80$ fs, mid-IR pulse energy $E_0 \approx 6.0$ mJ, and the energy of the second harmonic $E_{\rm SH} \approx 0.2$ mJ, focused into a gas cell filled with krypton (green solid line), air (pink dashed line), and N_2 (brown dotted line) at pressure p with a parabolic mirror with a focal length of ≈50 cm.

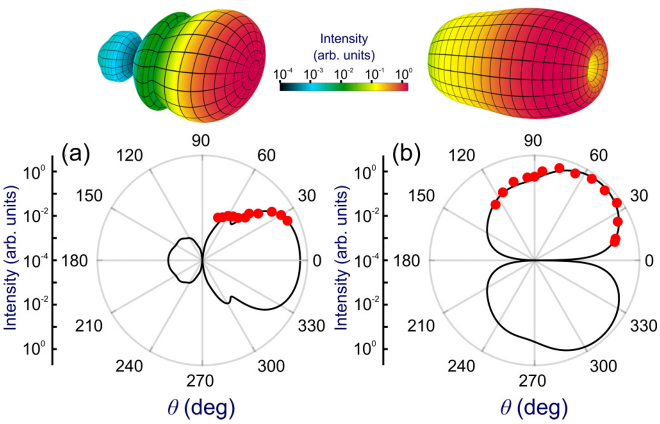

FIG. 9. The microwave output measured as a function of θ using the WCA5 (a) and WCA1 (b) detector set at $\varphi = 0^\circ$ in experiments with a two-color laser driver with $\lambda_0 \approx 3.9\,\mu$m, $E_0 \approx 15$ mJ, $\lambda_{\mathrm{SH}} = \lambda_0/2$, $E_{\mathrm{SH}} \approx 0.1$ mJ, $\phi_{\mathrm{SH}} = \pi/2$, and $\tau_0 \approx 80$ fs (a) and a single-color laser driver with $\lambda_0 \approx 3.9\,\mu$m, $E_0 \approx 15$ mJ, and $\tau_0 \approx 80$ fs (b) in a gas cell filled with air at $p \approx 1$ bar (a) and $p \approx 50$ mbar (b). Shown with the solid line are the best fits of experimental dependences with Eqs. (2), (3), and (7) with integration over the detection range of the respective WCA with $L = 2.2$ cm (a) and $L = 3.6$ cm (b). The three-dimensional microwave radiation patterns are shown at the top of the respective panels.

[2,45–47], had such features been detectable in the spectra, temporal traces, or radiation patterns of the microwave-THz output. Third, experiments within this variety of gases could help reveal meaningful correlations between the efficiency of microwave-THz generation and the ionization potential E_{g} of the gas target.

Experiments performed as a part of this study suggest that laser-ionization-assisted microwave-THz generation is a universal effect that occurs in both purely atomic and purely molecular gases [green solid and brown dotted lines in Fig. 8(d)], as well as in gas mixtures [pink dashed line in Fig. 8(d)]. Our experiments do not reveal any features of microwave-THz generation, e.g., any signatures of the Raman effect, that would be specific to a molecular optical nonlinearity. Finally, as a general tendency, gases with a lower ionization potential are found to provide a higher microwave-THz yield. Specifically, with the energy of 80-fs, 3.9-μm driver pulses set at $E_0 \approx 6.0$ mJ, microwave-THz radiation energies in the range of 20 μJ were achieved in experiments with Kr [$E_{\mathrm{g}} \approx 14.0$ eV, the green solid line in Fig. 8(d)]. The microwave-THz yield of laser-induced plasmas in molecular nitrogen, on the other hand, is appreciably lower [cf. the brown dotted and green solid lines in Fig. 8(d)], which correlates well with a higher ionization potential of N_2, $E_{\mathrm{g}} \approx 15.8$ eV.

IV. LASER-DRIVEN MICROWAVE-THz GENERATION: INSIGHTS FROM PULSED-ANTENNA ELECTRODYNAMICS

A. Driving current

Seeking to understand these experimental findings, we resort to the analysis of radiation patterns and polarization properties of laser-plasma emission as dictated by the symmetry of one- and two-color laser-plasma interaction settings. To this end, we consider an ultrashort laser pulse with a central frequency ω_0 that induces ultrafast ionization as it propagates through a transparent medium, giving rise to a steep ionization front, which rides on the back of the driver pulse, moving with a speed $v = c/n_0$, $n_0 = n_g(\omega_0)$ being the group index at frequency ω_0. Electric currents $\mathbf{J}_{\mathrm{p}}(t–z/v)$ induced in the wake of the driver pulse, with the z axis chosen along the driver propagation direction, provide a source of secondary radiation [38–40,48].

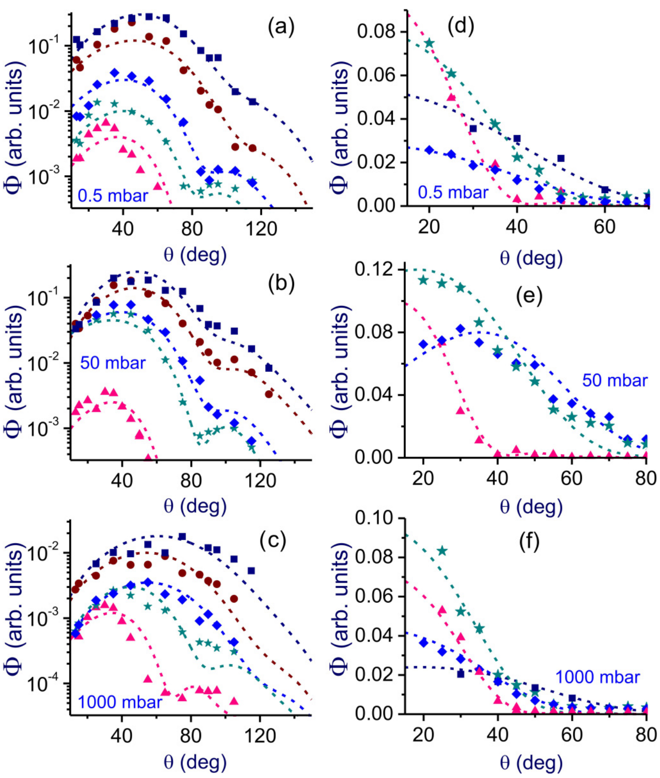

FIG. 10. The microwave output measured as a function of θ in experiments with single-color laser driver with $\lambda_0 \approx 3.9\,\mu$m, $E_0 \approx 15$ mJ, and $\tau_0 \approx 80$ fs (a–c) and two-color laser driver with $\lambda_0 \approx 3.9\,\mu$m, $E_0 \approx 15$ mJ, $\lambda_{\mathrm{SH}} = \lambda_0/2$, $E_{\mathrm{SH}} \approx 0.1$ mJ, $\phi_{\mathrm{SH}} = \pi/2$, and $\tau_0 \approx 80$ fs (d–f) in a gas cell filled with air at $p \approx 0.5$ mbar (a,d), 50 mbar (b,e), and 1000 mbar (c,f) with microwave detectors designed for different frequency ranges: WCA1 (navy boxes), WCA2 (brown circles), WCA3 (blue diamonds), WCA4 (cyan stars), and WCA5 (pink triangles). All the WCAs are set at $\varphi = 0^\circ$. Shown with the dashed line is the best fit of experimental dependences with Eq. (2) (a–c) and Eq. (7) (d–f) with integration over the detection range of the respective WCA detector.

The spatiotemporal symmetry of the laser driver—a predominantly transverse-field waveform, whose extension in space and time is confined by the beam size and the pulse width—suggests a generic view of $\mathbf{J}_{\mathrm{p}}$ as a sum, $\mathbf{J}_{\mathrm{p}} = \mathbf{J}_{\mathrm{l}} + \mathbf{J}_{\mathrm{t}}$, of a longitudinal current $\mathbf{J}_{\mathrm{l}}$, oriented along the z axis [Figs. 1 and 7(c)], and a transverse current $\mathbf{J}_{\mathrm{t}}$, lying in the plane perpendicular to the z axis (the xy plane), i.e., the plane spanned by the electric and magnetic fields of the laser driver. The symmetry of $\mathbf{J}_{\mathrm{l}}$ and $\mathbf{J}_{\mathrm{t}}$ translates, via the current-radiation-field map as dictated by equations of electrodynamics [49], into the symmetry of polarization modes and signature radiation patterns of secondary emission. The key properties of this map can be understood by viewing electromagnetic radiation by a laser plasma of length L at space-time point $(\mathbf{r}, t)$ as a superposition of radiation by all current elements

$$\mathbf{j}(\mathbf{r},\ t) = \mathbf{j}_0(\eta)\delta(\rho)[\Theta(z) - \Theta(z - L)], \tag{1}$$

within L, with $\eta = z–vt$, $\rho = (x, y)$, the Dirac delta function $\delta(\rho)$, and the Heaviside step function $\Theta(\xi)$.

B. Laser-plasma antennas and Cherenkov radiation

It is instructive to note that, with the current $\mathbf{j}_0(\eta) = (j_{0x}(\eta),\ j_{0y}(\eta),\ j_{0z}(\eta))$ taken in the form of $\mathbf{j}_0(\eta) = (0, 0, ev\delta(z–vt))$, where e is the electron charge, $\mathbf{j}(\mathbf{r}, t)$ becomes the current used in the canonical Frank-Tamm model of Cherenkov radiation [50,51]. Defining $\mathbf{j}_0(\eta)$ as $\mathbf{j}_0(\eta) = (0, 0, ev\delta(z–vt))$, on the other hand, we arrive at a model of an impulsively driven antenna [52]. In both cases, the current is purely longitudinal, its only nonzero component being $j_0(\eta) = j_{0z}(\eta)$, giving rise to electromagnetic radiation whose vector potential $\mathbf{A}$ is along the z axis and whose pronounced cylindrical symmetry is best appreciated in the cylindrical system of coordinates (ρ, θ, z). In this system of coordinates, the radiation field is fully described by three field components —E_ρ, E_z, and H_θ.

Had the path L been infinite, a charge moving with a constant speed $\mathbf{v}$ with no acceleration whatsoever could only radiate via the Cherenkov effect, giving rise to a signature conical emission at an angle $\theta_0 = \arccos[1/(\beta n)]$ relative to the z axis, with $\beta = v/c$ and $n = n(\omega)$ being the refractive index at radiation frequency ω. Such radiation can only make it to the far field when $\beta n > 1$, becoming evanescent when $v < c/n$. For finite L, however, the model of Eq. (1) implies that the current $\mathbf{j}_0(\eta)$ builds up near the front edge of the plasma, at $z = 0$, and fades away at its rear edge, at $z = L$, with the charges accelerated at $z = 0$, to acquire their velocity $\mathbf{v}$, and decelerated at $z = L$, to be brought to a halt. Integration of the radiation field emitted by the current (1) over the path L gives for the far-field radiation pattern at a distance $R \gg L$ from the plasma source,

$$S_l(\omega, \theta, L) \propto \frac{e^2\beta^2}{4\pi^2 c R_0^2}[Q(\omega, \theta, L)]^2 \sin^2\theta, \tag{2}$$

where

$$Q(\omega, \theta, L) = \frac{\sin\left[\frac{\omega L}{2v}(1 - \beta n\cos\theta)\right]}{1 - \beta n\cos\theta}. \tag{3}$$

As an important insight, the angular dependence of the factor $Q(\omega,\ \theta,\ L)$ in Eq. (3) can be understood either as a result of coherently combined radiation by accelerating and decelerating charges near the plasma edges or as Cherenkov radiation by charges within a finite path L. The signature Cherenkov emission cone is recovered from Eqs. (2) and (3) via $\lim_{L\to\infty}[Q(\omega,\ \theta,\ L)] = \pi\delta(1–\beta n\cos\theta)$. The radiation output in this regime vanishes unless $v > c/n$ and $\cos\theta = \cos\theta_0 = 1/(\beta n)$, accurately reproducing all the properties of Cherenkov radiation by superluminal $v > c/n$ charges.

When L is finite, however, the translational symmetry of the radiation source is lost. As one significant consequence, radiation emission is no longer a prerogative of superluminal $v > c/n$ charges, but can also be emitted by subluminal currents, i.e., currents with $v < c/n$. In this setting, the radiation field induced by $v < c/n$ charges ceases to be evanescent, with Eqs. (2) and (3) providing a continuous and analytical crossover from the superluminal to the subluminal regime of charge-current radiation. As a part of this crossover, the angle corresponding to the maximum of $S(\omega,\ \theta,\ L)$ for radiation by subluminal $v < c/n$ charges can be recovered from the evanescent-field, $\beta n < 1$ extension of the Cherenkov emission angle, $\sin\theta_0 = i[1/(\beta n)^2–1]^{1/2}$ [53].

C. Longitudinal and transverse currents

Since the current in Eq. (1) builds up via an acceleration of charges at $z = 0$ and wanes through a symmetric deceleration that stops charges at $z = L$, useful insights into the properties of the angular distribution $S(\omega,\ \theta,\ L)$ are gained via the textbook equations [49,54]

$$\mathbf{E} \approx (e/c)\{\mathbf{n} \times [(\mathbf{n} - \boldsymbol{\beta}) \times (\mathbf{a}/c)]/[(1 - \boldsymbol{\beta}\cdot\mathbf{n})^3 R_0]\}_{\text{ret}} \tag{4}$$

and

$$\mathbf{B} = [\mathbf{n} \times \mathbf{E}]_{\text{ret}}, \tag{5}$$

for the radiation field emitted by a charge e moving with a normalized velocity $\boldsymbol{\beta} = \mathbf{v}/c$ and acceleration $\mathbf{a}$ and detected at $\mathbf{r} = R_0\mathbf{n}$ in the far field.

When $\mathbf{a}$ is parallel or antiparallel to $\mathbf{v}$, as would be the case for a longitudinal current $\mathbf{J}_l$, where charges accelerate near $z = 0$ and decelerate near $z = L$, the energy flux along the z axis is zero, as $\boldsymbol{\beta} \times \mathbf{a} = 0$ and $\mathbf{n} \times \mathbf{a} = 0$. In a more general case of $\theta \neq 0$, the radiation power emitted by such charges per unit solid angle,

$$(dP/d\Omega)_b = c|R\mathbf{E}|^2\big/(4\pi) = \frac{e^2\beta^2}{4\pi^2 c}\frac{\sin^2\theta}{(1 - \beta n\cos\theta)^2}, \tag{6}$$

is readily recognizable as the radiation power of bremsstrahlung per unit solid angle [49,54].

It is straightforward to see now, from Eqs. (2)–(6), that the radiation pattern of a plasma current of length L connects to $(dP/d\Omega)_b$ via $S(\omega,\ \theta,\ L) \propto R_0^{-2}(dP/d\Omega)_b \sin[\phi(L)]$, with $\varphi(L) = (\omega L/v)(1–\beta n\cos\theta)$, articulating the role of radiation by currents accelerating at $z = 0$ and decelerating at $z = L$. It is also readily seen now that the $\sin^2\theta$ factor in $(dP/d\Omega)_b$ and, hence, in $S(\omega,\ \theta,\ L)$ for $\mathbf{J}_l$ is inherited from the $[\mathbf{n} \times \mathbf{a}]^2 = |\mathbf{a}|^2\sin^2\theta$ product in Eq. (4), showing that a charge whose acceleration, $\mathbf{a}$, is parallel or antiparallel to its velocity, $\mathbf{v}$, does not radiate in the direction of $\mathbf{v}$, that is, at $\theta = 0$ in our setting [Fig. 9(b)].

In a transverse current, the current buildup at $z = 0$ sets charges in motion in a direction perpendicular to $\mathbf{v}$, while current fading at $z = L$ stops this motion. In this setting,

$[\mathbf{n}\times\mathbf{a}]^2 = |\mathbf{a}|^2\cos^2\theta$, leading to

$$S_t(\omega,\theta,L) \propto \frac{e^2\beta^2}{4\pi^2 cR_0^2}[Q(\omega,\theta,L)]^2\cos^2\theta. \tag{7}$$

Moreover, transverse currents $\mathbf{J}_{\mathrm{t}}$ with a well-defined orientation in the xy plane, e.g., along the driver field, emit linearly polarized radiation. The readout Φ of a polarization-sensitive detector, such as a WCA, will then follow a $\cos\varphi$ behavior as a function of the angle φ that its **E**-field probe, e.g., the coaxial cable of a WCA, makes with $\mathbf{J}_{\mathrm{t}}$. This φ dependence of Φ is in stark contrast with its behavior in the case of radially polarized emission from a longitudinal current, which translates into no φ dependence whatsoever.

D. Cherenkov-cone radiation-pattern structure

Due to the dispersion of the refractive index $n = n(\omega)$ and the group index $n_{\mathrm{g}} = n_{\mathrm{g}}(\omega)$, as dictated by causality, the angle $\theta_0 = \arccos[1/(\beta n)]$ of the Cherenkov emission cone is a function of both the frequency ω of microwave-THz radiation and the central frequency of the laser driver. With the central frequency of the laser driver fixed at ω_0, the Cherenkov-cone angle for microwave-THz radiation with frequency ω is $\theta_0 = \theta_0(\omega,\mathcal{R}) = \arccos[n_0(\mathcal{R})/n(\omega,\mathcal{R})]$, where $n_0(\mathcal{R}) = n_g(\omega_0,\mathcal{R})$ and is the set of physical parameters that defines the optical properties of a gas medium. Specifically, for atmospheric air, the standard choice of $\mathcal{R}$ would be $\mathcal{R} = \{T, h, \rho\}$, where T is the temperature, h is the humidity, and ρ is the content of CO_2.

Shown in Fig. 7(d) is the Cherenkov-cone angle $\theta_0(\omega,\mathcal{R})$ for atmospheric air at $T = 25\,^\circ\mathrm{C}$, $\rho = 50\%$, $p = 1$ bar, and $h = 0\%$ (green solid line), 50% (blue dashed line), and 100% (pink dotted line) $T = 25\,^\circ\mathrm{C}$, with the central wavelength of the laser driver chosen in such a way as to relate to our experiments, $\lambda_0 = 2\pi c/\omega_0 = 3.9\,\mu\mathrm{m}$. For this set of parameters, the Cherenkov-cone angle θ_0 is seen to be less than $1\,^\circ$ within the entire range of microwave frequencies studied in our experiments, all the way up to $\nu = \omega/(2\pi) \approx 0.5$ THz. This result implies that, within this frequency range, the speed of the microwave radiation source, $v = c/n_g(\omega_0)$, is close to the phase velocity of microwave radiation, $u = c/n(\omega)$. The product $\beta n(\omega)$ in Eqs. (2), (3), (6), and (7) is then, to a good approximation, $\beta n \approx 1$. In the case of transverse plasma currents, $\beta n \approx 1$ in Eqs. (3) and (7) will favor microwave emission in the forward direction, in full agreement with experiments [Figs. 9(a) and 10(d)–10(f)]. For longitudinal currents, on the other hand, radiation in the forward direction is still surprised, even with $\beta n \approx 1$, because, $\boldsymbol{\beta}\times\mathbf{a} = 0$ and $\mathbf{n}\times\mathbf{a} = 0$ for such currents if $\mathbf{n}$ is in the forward direction. This intuition is also consistent with experiments [Figs. 9(b) and 10(a)–10(c)].

E. Pulsed-antenna radiation: Spatial structure and angular dispersion

With $S(\omega,\ \theta,\ L) \propto R_0^{-2}(dP/d\Omega)_b\sin[\phi(L)]$ establishing a physically insightful connection between radiation by laser-driven plasma currents and radiation by accelerated charges, the multiplier $\sin[\phi(L)]$ in Eqs. (2) and (7) is readily recognized as a factor that includes the phase shift between radiation emitted by the charges accelerating at $z = 0$ and radiation with the same amplitude, polarization, and radiation pattern originating from the charges decelerating at $z = L$.

As a useful pulsed-antenna perspective on this factor, radiation emitted by $\mathbf{J}_{\mathrm{l}}$ or $\mathbf{J}_{\mathrm{t}}$ at any space-time point $(\mathbf{r},\ t)$ in the far field can be viewed as a superposition of two spatially separated spherical waves, S_1 and S_2, emanating from, respectively, $z = 0$ $z = 0$ and $z = L$ [Fig. 7(c)]. The radiation field at each point $\mathbf{r}$ is thus a sum of two waveforms of opposite polarity [Fig. 7(c)] separated by a delay time $\Delta t = (L/v)(1–\beta n\cos\theta)$. Such a structure of radiation field around the free ends of an impulsively driven wire antenna is known since at least the seminal work by Heaviside [55]. In a more recent work in the literature, radiation patterns of this class have been studied in the context of transient electromagnetism, focused on understanding the time-domain picture of antenna radiation and radiation scattering from transmission lines [56,57]. That edge effects tend to couple Cherenkov radiation from an ultrafast photoionization front in laser-induced filaments and laser-driven plasmas to bremsstrahlung and transition radiation has been recently shown in Ref. [58].

V. LASER-PLASMA MICROWAVE ANTENNAS: MODELING VERSUS EXPERIMENTS

A. Microwave power as a function of the distance from the plasma source

In Figs. 7(a), 7(b), 8(a)–8(c), 9(a), 9(b), and 10(a)–10(f), predictions of Eqs. (2) and (7) are plotted against the results of one- and two-color laser-plasma experiments. Overall, the physical model based on these equations is seen to provide a meaningful fit for the entire set of the available experimental data. Specifically, the best fit for microwave radiation patterns is achieved [Figs. 9(a) and 9(b)] with plasma-current lengths L that agree very well with L values found from experiments, $L = 2.2$ cm for the conditions of experiments presented in Fig. 9(a) and $L = 3.6$ cm for the experiment in Fig. 9(b). The plasma-current length L is found to display a complex, nonmonotonic behavior as a function of the gas pressure p. For low electron densities n_{e}, higher p tend to translate into larger L. For higher n_{e}, however, the current length scale L first saturates and then starts decreasing with a further growth in p due to plasma absorption, plasma refraction, and spatial-self-action-induced beam instabilities [37,45,46,59].

The microwave readout Φ is found to closely follow the $1/R_0^2$ scaling with the distance R_0 from the laser-plasma source within the entire range of gas pressures and for all the WCA detectors used for Φ analysis in both one- and two-color laser-plasma experiments [Figs. 7(a) and 7(b)]. This scaling is fully consistent with the far-field physical picture of microwave generation in our laser-plasma setting as phase-shifted spherical waves of impulsively driven, transient-current-fed antenna radiation [note the $1/R_0^2$ factor in Eqs. (2) and (7)].

B. Polarization mode structure

The pulsed-antenna view of microwave radiation by laser-driven plasmas also offers useful insights into polarization properties and radiation patterns of microwave emission observed in our laser-plasma studies. Specifically, in single-color experiments, the E_r component of the microwave field [pink filled triangles in Figs. 8(a) and 8(b)] is independent of φ within the entire range of gas pressures studied in our experiments and is orders of magnitude stronger than its orthogonal counterpart E_φ [green open triangles in Figs. 8(a) and 8(b)]. Such a polarization structure of the microwave output is fully consistent with the view of microwave generation as radiation of a longitudinal-current-fed pulsed antenna. The vector potential in such a radiation field is along the z axis, as dictated by the spatial symmetry of $\mathbf{J}_l$, giving rise to an electric field with $E_\varphi = 0$ and φ-independent E_r.

Microwave radiation with drastically different polarization properties is observed in experiments with a two-color driver [Fig. 8(c)]. Due to its broken time symmetry [8], such a two-color field induces efficient transverse photoionization currents that do not cancel within the field cycle, as would be the case in experiments with a long, many-cycle single-color driver pulse. Such transverse currents are expected to give rise to a linearly polarized mode of microwave radiation [Fig. 8(c)]. In full agreement with this symmetry argument, both the E_r and E_φ field components of microwave radiation generated in our two-color laser-plasma studies were found to closely follow a signature figure-of-eight φ dependence [Fig. 8(c)], clearly indicating the linear polarization of the microwave field. Polarization of microwave radiation thus bears clear signatures of the symmetry of transient plasma currents, thus offering means to resolve the spatial structure of laser-driven plasma currents and providing much-needed insights into an ultrafast physics of laser-plasma interaction.

C. Radiation patterns and angular dispersion

When viewed from the pulsed-antenna perspective, microwave generation in one- and two-color laser-plasma settings is understood as radiation by a pulsed antenna fed by either longitudinal or transverse plasma currents. As can be seen from Figs. 9(a), 9(b), and 10(a)–10(f), Eqs. (2) and (7), which serve as an analytic expression of this view, provide an accurate description of microwave radiation patterns $\Phi(\theta)$ observed in both one- and two-color experiments within a broad range of microwave frequencies and gas pressures. Specifically, the $\Phi(\theta)$ profiles measured in one-color experiments [Figs. 9(b) and 10(a)–10(c)] are seen to exhibit well-resolved dips in the direction of driver propagation ($\theta = 0$) along with pronounced off-axial peaks, which tend to shift toward larger θ for WCAs designed for lower-frequency microwaves.

This tendency is readily understood from the pulsed-antenna perspective, by viewing microwave field waveforms detected by each WCA in our experiments as a superposition of spherical waves [S_1 and S_2 in Fig. 7(c)] emitted by accelerating and decelerating charges at the antenna's end points. A detector placed in the far field, $R_0 \gg L$, at an angle θ relative to the driver propagation direction will then register field waveforms whose crests and troughs are separated by $\Delta L = c\Delta t = (cL/v)(1–\beta n\cos\theta)$. Such a crest-trough separation translates into a central wavelength of $\lambda = 2c\Delta t = 2c(L/u)(1–\beta n\cos\theta)$, as adequately captured by Eqs. (2) and (7). A detector placed at larger θ will thus register longer-λ field waveforms. This tendency is also clearly manifested in the spectra of microwave radiation measured at different θ angles (Fig. 4).

D. Wide-angle microwave radiation

As can be readily seen from these measurements, the readings of WCA detectors designed for higher microwave frequencies decrease much faster with an increase in θ than the readings of WCAs intended for lower ω. Eventually, for large, obtuse θ outside the broadside plane, only the lowest-ω radiation components remain detectable in the laser-plasma microwave output [Figs. 4(i) and 4(j)]. As one of the central results of this study, radiation patterns of such lowest-ω emission [$\nu = \omega/(2\pi) < 10\,\mathrm{GHz}$ in Figs. 4(a)–4(j)] are found to extend to obtuse θ angles well beyond the broadside plane [Figs. 4(i) and 4(j)].

Analysis of the angular profiles $\Phi(\theta)$ of $\nu < 10\,\mathrm{GHz}$ radiation shows that much of this radiation flux is emitted at angles $\theta > 125^\circ$ relative to the direction of the laser driver [Figs. 10(a)–10(c)]. These results are also fully consistent with the physical picture of microwave radiation by an impulsively driven laser-plasma antenna [cf. data points and the dashed lines in Figs. 10(a)–10(c)], which suggests that lower-ω radiation is emitted at larger θ angles. Measurements with the Golay-cell detector and microwave-THz filter stacks show that, with the energy of 80-fs mid-IR driver pulses set at ≈15 mJ, obtuse-angle microwave radiation energies in the range of a few microjoules can be achieved.

Laser methods enabling a remotely driven generation of electromagnetic field waveforms with such ultrawide radiation patterns are in great demand in remote sensing and standoff detection applications [60–65]. The laser-plasma setting demonstrated in this study offers promising approaches to confront this challenge as it suggests a compact arrangement whereby a laser-plasma source of bright, ultrawide-angle microwave-THz radiation could be created with a remote, e.g., ground-based, laser driver, giving rise to intense microwave-THz emission at obtuse angles well beyond the broadside plane, thus providing a powerful resource for remote sensing and standoff detection of trace gases, microdroplets, and aerosols in the atmosphere and at remote surfaces.

VI. CONCLUSION

To summarize, transient electric currents driven by high-peak-power midinfrared laser pulses have been shown to provide a source of broadband, wide-angle microwave radiation, whose spectral, spatial, and polarization properties can be adequately understood from a perspective of impulsively driven antenna radiation. When suitably tailored, such laser-driven antennas are shown to generate bright microwave pulses with energies in the range of tens of microjoules and ultrawide-angle radiation patterns extending to obtuse angles well beyond the broadside plane, with a considerable radiation flux detected at angles $\theta > 125^\circ$ relative to the direction of the driver beam. Polarization of microwave radiation from laser-driven plasmas is shown to bear clear signatures of the symmetry of transient plasma currents, providing a sensitive probe for ultrafast laser-plasma interactions.

ACKNOWLEDGMENTS

This research was supported in part by the Russian Foundation for Basic Research (Projects No. 20-21-00131 and No. 20-21-00140), Russian Science Foundation (Project No. 19-72-10054 – high-power nonlinear optics; Project No. 20-12-00088 – ultrabroadband optical science), and the Welch Foundation (Grant No. A-1801-20180324). Research of M.V.R. is partially supported by the Russian Foundation for Basic Research (Project No. 20-32-90228).

[1] P. Gibbon, *Short Pulse Laser Interactions with Matter* (Imperial College, London, 2005).

[2] A. M. Zheltikov and N. I. Koroteev, Coherent four-wave mixing in excited and ionized gas media: Four-photon spectrochronography, ellipsometry, and nonlinear-optical imaging of atoms and ions, Usp. Fiz. Nauk **169**, 385 (1999) [Phys.-Usp. **42**, 321 (1999)].

[3] U. Teubner and P. Gibbon, High-order harmonics from laser-irradiated plasma surfaces, Rev. Mod. Phys. **81**, 445 (2009).

[4] C. Thaury and F. Quéré, High-order harmonic and attosecond pulse generation on plasma mirrors: Basic mechanisms, J. Phys. B: At., Mol. Opt. Phys. **43**, 213001 (2010).

[5] T. Tajima and J. M. Dawson, Laser Electron Accelerator, Phys. Rev. Lett. **43**, 267 (1979).

[6] V. Malka, S. Fritzler, E. Lefebvre, M.-M. Aleonard, F. Burgy, J.-P. Chambaret, J.-F. Chemin, K. Krushelnick, G. Malka, S. Mangles *et al.*, Electron acceleration by a wake field forced by an intense ultrashort laser pulse, Science **298**, 1596 (2002).

[7] W. P. Leemans, B. Nagler, A. J. Gonsalves, C. Tóth, K. Nakamura, C. G. R. Geddes, E. Esarey, C. B. Schroeder, and S. M. Hooker, GeV electron beams from a centimetre-scale accelerator, Nat. Phys. **2**, 696 (2006).

[8] V. Malka, J. Faure, Y. A. Gauduel, E. Lefebvre, A. Rousse, and K. T. Phuoc, Principles and applications of compact laser–plasma accelerators, Nat. Phys. **4**, 447 (2008).

[9] E. Esarey, C. B. Schroeder, and W. P. Leemans, Physics of laser-driven plasma-based electron accelerators, Rev. Mod. Phys. **81**, 1229 (2009).

[10] Steinke, J. van Tilborg, C. Benedetti, C. G. R. Geddes, C. B. Schroeder, J. Daniels, K. K. Swanson, A. J. Gonsalves, K. Nakamura, N. H. Matlis, B. H. Shaw, E. Esarey, and W. P. Leemans, Multistage coupling of independent laser-plasma accelerators, Nature (London) **530**, 190 (2016).

[11] C. Geddes, C. Toth, J. Van Tilborg, E. Esarey, C. Schroeder, D. Bruhwiler, C. Nieter, J. Cary, and W. Leemans, High-quality electron beams from a laser wakefield accelerator using plasma-channel guiding, Nature (London) **431**, 538 (2004).

[12] G. A. Mourou, T. Tajima, and S. V. Bulanov, Optics in the relativistic regime, Rev. Mod. Phys. **78**, 309 (2006).

[13] J. Faure, Y. Glinec, A. Pukhov, S. Kiselev, S. Gordienko, E. Lefebvre, J.-P. Rousseau, F. Burgy, and V. Malka, A laser-plasma accelerator producing monoenergetic electron beams, Nature (London) **431**, 541 (2004).

[14] S. P. Mangles, C. Murphy, Z. Najmudin, A. G. R. Thomas, J. Collier, A. E. Dangor, E. Divall, P. Foster, J. Gallacher, C. Hooker, D. A. Jaroszynski, A. J. Langley, W. B. Mori, P. A. Norreys, F. S. Tsung, R. Viskup, B. R. Walton, and K. Krushelnick, Monoenergetic beams of relativistic electrons from intense laser–plasma interactions, Nature (London) **431**, 535 (2004).

[15] J. Fuchs, P. Antici, E. D'Humieres, E. Lefebvre, M. Borghesi, E. Brambrink, C. A. Cecchetti, M. Kaluza, V. Malka, M. Manclossi, S. Meyroneinc, P. Mora, J. Schreiber, T. Toncian, H. Perpin, and P. Audebert, Laser-driven proton scaling laws and new paths towards energy increase, Nat. Phys. **2**, 48 (2006).

[16] B. Dromey, M. Zepf, A. Gopal, K. Lancaster, M. S. Wei, K. Krushelnick, M. Tatarakis, N. Vakakis, S. Moustaizis, R. Kodama, M. Tampo, C. Stoeckl, R. Clarke, H. Habara, D. Neely, S. Karsch, and P. Norreys, High harmonic generation in the relativistic limit, Nat. Phys. **2**, 456 (2006).

[17] A. Tarasevitch, K. Lobov, C. Wünsche, and D. von der Linde, Transition to the Relativistic Regime in High Order Harmonic Generation, Phys. Rev. Lett. **98**, 103902 (2007).

[18] D. Guénot, D. Gustas, A. Vernier, B. Beaurepaire, F. Böhle, M. Bocoum, M. Lozano, A. Jullien, R. Lopez-Martens, A. Lifschitz, and J. Faure, Relativistic electron beams driven by kHz single-cycle light pulses, Nat. Photonics **11**, 293 (2017).

[19] A. V. Mitrofanov, D. A. Sidorov-Biryukov, M. V. Rozhko, S. V. Ryabchuk, A. A. Voronin, and A. M. Zheltikov, High-order harmonic generation from a solid-surface plasma by relativistic-intensity sub-100-fs mid-infrared pulses, Opt. Lett. **43**, 5571 (2018).

[20] P. Agostini and L. F. DiMauro, The physics of attosecond light pulses, Rep. Prog. Phys. **67**, 813 (2004).

[21] P. B. Corkum and F. Krausz, Attosecond science, Nat. Phys. **3**, 381 (2007).

[22] B. Dromey, S. Rykovanov, M. Yeung, R. Hörlein, D. Jung, D. C. Gautier, T. Dzelzainis, D. Kiefer, S. Palaniyppan, R. Shah, J. Schreiber, H. Ruhl, J. C. Fernandez, C. L. S. Lewis, M. Zepf, and B. M. Hegelich, Coherent synchrotron emission from electron nanobunches formed in relativistic laser-plasma interactions, Nat. Phys. **8**, 804 (2012).

[23] J. M. Mikhailova, M. V. Fedorov, N. Karpowicz, P. Gibbon, V. T. Platonenko, A. M. Zheltikov, and F. Krausz, Isolated Attosecond Pulses from Laser-Driven Synchrotron Radiation, Phys. Rev. Lett. **109**, 245005 (2012).

[24] A. V. Mitrofanov, D. A. Sidorov-Biryukov, P. B. Glek, M. V. Rozhko, E. A. Stepanov, A. D. Shutov, S. V. Ryabchuk, A. A. Voronin, A. B. Fedotov, and A. M. Zheltikov, Chirp-controlled high-harmonic and attosecond-pulse generation via coherent-wake plasma emission driven by mid-infrared laser pulses, Opt. Lett. **45**, 750 (2020).

[25] K. Y. Kim, A. J. Taylor, J. H. Glownia, and G. Rodriguez, Coherent control of terahertz supercontinuum generation in ultrafast laser-gas interactions, Nat. Photonics **2**, 605 (2008).

[26] A. B. Fedotov, S. M. Gladkov, N. I. Koroteev, and A. M. Zheltikov, Highly efficient frequency tripling of laser radiation in a low-temperature laser-produced gaseous plasma, J. Opt. Soc. Am. B **8**, 363 (1991).

[27] A. J. Verhoef, A. V. Mitrofanov, E. E. Serebryannikov, D. V. Kartashov, A. M. Zheltikov, and A. Baltuska, Optical Detection of Tunneling Ionization, Phys. Rev. Lett. **104**, 163904 (2010).

[28] T. Balčiūnas, D. Lorenc, M. Ivanov, O. Smirnova, A. M. Zheltikov, D. Dietze, K. Unterrainer, T. Rathje, G. G. Paulus, A. Baltuška, and S. Haessler, CEP-stable tunable THz-emission originating from laser-waveform-controlled sub-cycle plasma-electron bursts, Opt. Express **23**, 15278 (2015).

[29] T. Balciunas, A. J. Verhoef, A. V. Mitrofanov, G. Fan, E. E. Serebryannikov, M. Y. Ivanov, A. M. Zheltikov, and A. Baltuska, Optical and terahertz signatures of subcycle tunneling dynamics, Chem. Phys. **414**, 92 (2013).

[30] D. Jang, R. M. Schwartz, D. Woodbury, J. Griff-McMahon, A. H. Younis, H. M. Milchberg, and K.-Y. Kim, Efficient terahertz and Brunel harmonic generation from air plasma via mid-infrared coherent control, Optica **6**, 1338 (2019).

[31] A. A. Voronin and A. M. Zheltikov, Laser-driven tunneling photocurrent as a source of midinfrared to microwave multidecade supercontinua yoked to high-order harmonics, Phys. Rev. A **101**, 043813 (2020).

[32] E. E. Serebryannikov, A. J. Verhoef, A. Mitrofanov, A. Baltuska, and A. M. Zheltikov, Signatures of attosecond electron tunneling dynamics in the evolution of intense few-cycle light pulses, Phys. Rev. A **80**, 053809 (2009).

[33] A. V. Mitrofanov, D. A. Sidorov-Biryukov, M. M. Nazarov, A. A. Voronin, M. V. Rozhko, A. D. Shutov, S. V. Ryabchuk, E. E. Serebryannikov, A. B. Fedotov, and A. M. Zheltikov, Ultraviolet-to-millimeter-band supercontinua driven by ultrashort mid-infrared laser pulses, Optica **7**, 15 (2020).

[34] A. Zheltikov, Multioctave supercontinua and subcycle lightwave electronics [Invited], J. Opt. Soc. Am. B **36**, A168 (2019).

[35] E. E. Serebryannikov and A. M. Zheltikov, Quantum and Semiclassical Physics behind Ultrafast Optical Nonlinearity in the Midinfrared: The Role of Ionization Dynamics within the Field Half Cycle, Phys. Rev. Lett. **113**, 043901 (2014).

[36] A. Englesbe, J. Elle, R. Reid, A. Lucero, H. Pohle, M. Domonkos, S. Kalmykov, K. Krushelnick, and A. Schmitt-Sody, Gas pressure dependence of microwave pulses generated by laser-produced filament plasmas, Opt. Lett. **43**, 4953 (2018).

[37] A. V. Mitrofanov, D. A. Sidorov-Biryukov, M. M. Nazarov, A. A. Voronin, M. V. Rozhko, A. B. Fedotov, and A. M. Zheltikov, Coherently enhanced microwave pulses from midinfrared-driven laser plasmas, Opt. Lett. **46**, 1081 (2021).

[38] P. Sprangle, J. Peñano, B. Hafizi, and C. Kapetanakos, Ultrashort laser pulses and electromagnetic pulse generation in air and on dielectric surfaces, Phys. Rev. E **69**, 066415 (2004).

[39] C. D'Amico, A. Houard, M. Franco, B. Prade, A. Mysyrowicz, A. Couairon, and V. T. Tikhonchuk, Conical Forward THz Emission from Femtosecond-Laser-Beam Filamentation in Air, Phys. Rev. Lett. **98**, 235002 (2007).

[40] C. D'Amico, A. Houard, S. Akturk, Y. Liu, J. Le Bloas, M. Franco, B. Prade, A. Couairon, V. Tikhonchuk, and A. Mysyrowicz, Forward THz radiation emission by femtosecond filamentation in gases: Theory and experiment, New J. Phys. **10**, 013015 (2007).

[41] A. M. Zheltikov, Let there be white light: Supercontinuum generation by ultrashort laser pulses, Phys.-Usp. **49**, 605 (2006).

[42] A. V. Mitrofanov, A. A. Voronin, M. V. Rozhko, D. A. Sidorov-Biryukov, M. M. Nazarov, A. B. Fedotov, and A. M. Zheltikov, Polarization and spatial mode structure of mid-infrared-driven terahertz-to-microwave radiation, ACS Photonics **8**, 1988 (2021).

[43] A. V. Mitrofanov, A. A. Voronin, D. A. Sidorov-Biryukov, S. I. Mitryukovsky, A. B. Fedotov, E. E. Serebryannikov, D. V. Meshchankin, V. Shumakova, S. Ališauskas, A. Pugžlys, V. Ya. Panchenko, A. Baltuška, and A. M. Zheltikov, Subterawatt few-cycle mid-infrared pulses from a single filament, Optica **3**, 299 (2016).

[44] A. V. Mitrofanov, A. A. Voronin, M. V. Rozhko, D. A. Sidorov-Biryukov, A. B. Fedotov, A. Pugžlys, V. Shumakova, S. Ališauskas, A. Baltuška, and A. M. Zheltikov, Self-compression of high-peak-power mid-infrared pulses in anomalously dispersive air, Optica **4**, 1405 (2017).

[45] A. Couairon and A. Mysyrowicz, Femtosecond filamentation in transparent media, Phys. Rep. **441**, 47 (2007).

[46] L. Bergé, S. Skupin, R. Nuter, J. Kasparian, and J.-P. Wolf, Ultrashort filaments of light in weakly ionized, optically transparent media, Rep. Prog. Phys. **70**, 1633 (2007).

[47] A. M. Zheltikov, Microstructure optical fibers for a new generation of fiber-optic sources and converters of light pulses, Usp. Fiz. Nauk **177**, 737 (2007) [Phys. Usp. **50**, 705 (2007)].

[48] I. Thiele, R. Nuter, B. Bousquet, V. Tikhonchuk, S. Skupin, X. Davoine, L. Gremillet, and L. Bergé, Theory of terahertz emission from femtosecond-laser-induced microplasmas, Phys. Rev. E **94**, 063202 (2016).

[49] J. D. Jackson, *Classical Electrodynamics*, 3rd ed. (Wiley, New York, 1999).

[50] I. Frank and I. Tamm, Coherent visible radiation of fast electrons passing through matter, Dokl. Akad. Nauk SSSR **14**, 109 (1937).

[51] I. Tamm, Radiation emitted by uniformly moving electrons, J. Phys. (USSR) **1**, 439 (1939).

[52] G. S. Smith, On the interpretation for radiation from simple current distributions, IEEE Antennas Propag. Mag. **40**, 9 (1998).

[53] J. D. Lawson, Cherenkov radiation, "physical" and "unphysical," and its relation to radiation from an accelerated electron, Am. J. Phys. **33**, 1002 (1965).

[54] D. J. Griffiths, *Introduction to Electrodynamics*, 3rd ed. (Prentice Hall, Upper Saddle River, NJ, 1999).

[55] O. Heaviside, *Electromagnetic Theory* (Electrician Printing and Publishing, London, 1899); [(Chelsea, New York, 1971)].

[56] E. K. Miller, An exploration of radiation physics in electromagnetics, IEEE Int. Symp. Antennas Propag. **3**, 2048 (1997).

[57] G. S. Smith, Teaching antenna radiation from a time-domain perspective, Am. J. Phys. **69**, 288 (2001).

[58] A. M. Zheltikov, Bremsstrahlung, transition, and Cherenkov radiation by laser filaments, Phys. Rev. A **104**, 043509 (2021).

[59] A. A. Voronin and A. M. Zheltikov, Nonlinear dynamics of high-power ultrashort laser pulses: Exaflop computations on a laboratory computer station and subcycle light bullets, Usp. Fiz. Nauk **186**, 957 (2016) [Phys.-Usp. **59**, 869 (2016)].

[60] P. R. Hemmer, R. B. Miles, P. Polynkin, T. Siebert, A. V. Sokolov, P. Sprangle, and M. O. Scully, Standoff spectroscopy via remote generation of a backward-propagating laser beam, Proc. Natl. Acad. Sci. USA **108**, 3130 (2011).

[61] A. M. Zheltikov, M. N. Shneider, and R. B. Miles, Radar return enhanced by a grating of species-selective multiphoton ionization as a probe for trace impurities in the atmosphere, Appl. Phys. B **83**, 149 (2006).

[62] A. Dogariu, J. B. Michael, M. O. Scully, and R. B. Miles, High-gain backward lasing in air, Science **331**, 442 (2011).

[63] A. J. Traverso, R. Sanchez-Gonzales, L. Yuan, K. Wang, D. V. Voronine, A. M. Zheltikov, Y. Rostovtsev, V. A. Sautenkov, A. V. Sokolov, S. W. North, and M. O. Scully, Coherence brightened laser source for atmospheric remote sensing, Proc. Natl. Acad. Sci. USA **109**, 15185 (2012).

[64] P. N. Malevich, D. Kartashov, Z. Pu, S. Ališauskas, A. Pugžlys, A. Baltuška, L. Giniūnas, R. Danielius, A. A. Lanin, A. M. Zheltikov, M. Marangoni, and G. Cerullo, Ultrafast-laser-induced backward stimulated Raman scattering for tracing atmospheric gases, Opt. Express **20**, 18784 (2012).

[65] P. N. Malevich, R. Maurer, D. Kartashov, S. Ališauskas, A. A. Lanin, A. M. Zheltikov, M. Marangoni, G. Cerullo, A. Baltuška, and A. Pugžlys, Stimulated Raman gas sensing by backward UV lasing from a femtosecond filament, Opt. Lett. **40**, 2469 (2015).